THE JOURNAL OF PHYSICAL CHEMISTRY C
A JOURNAL OF THE AMERICAN CHEMICAL SOCIETY

pubs.acs.org/JPCC

Article

Grain Boundaries and Their Impact on Li Kinetics in Layered-Oxide Cathodes for Li-Ion Batteries

Xiaomei He, Hong Sun, Xiangdong Ding,* and Kejie Zhao*

Cite This: *J. Phys. Chem. C* 2021, 125, 10284−10294

Read Online

ACCESS | Metrics & More | Article Recommendations | Supporting Information

ABSTRACT: Defects are pervasive in electrochemical systems across multiple length scales. The defect chemistry largely differs from the bulk behavior and often dictates the rate performance for battery materials. However, the impact of material defects on Li kinetics remains elusive because of their complex nature and the sensitivity of the reaction kinetics on the local atomic environment. Here we focus on the grain boundaries (GBs) in layered-oxide cathodes and address their role in Li transport using the first-principles theoretical approach. We construct the coincidence site lattices of $\sum 2(1\bar{1}04)$, $\sum 3(\bar{1}102)$, $\sum 5(1\bar{1}01)$, and $\sum 9(1\bar{1}04)$ GBs. The energy profiles for Li migration across and along the grain planes are plotted. We discuss in detail how the atomistic features associated with various grain structures such as the local structural distortion and charge redistribution determine the Li transport kinetics. Specifically, the coherent $\sum 2$ GBs facilitate Li migration with 1−2 orders of magnitude increased diffusivity than the bulk diffusion, the asymmetric $\sum 3$ GBs significantly impede Li diffusion, and the locally disordered $\sum 5$ and $\sum 9$ GBs cause slightly increased Li diffusivity at the intermediate diffusion distance (∼15 Å). We further evaluate the overall Li diffusivity and conductivity in the layered-oxide lattice by a distinction of Li transport in the bulk, across the GBs, and along the grain planes. The fundamental understanding sheds insight on a prevalent defect in the state-of-the-art cathode and its potential optimization of Li kinetics.

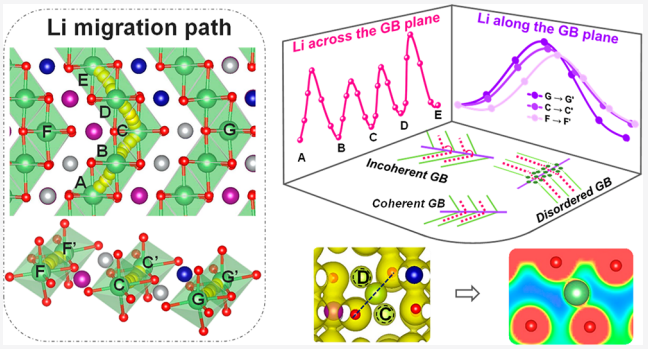

1. INTRODUCTION

Li-ion batteries (LIBs) emerge as the most prominent choice of modern energy storage technologies. The flourishing electric vehicle industry and the ever-increasing demand of long duration and fast charging of portable electronics drive LIBs toward high energy density, high-rate performance, and long cyclic stability.[1,2] The battery performance is fundamentally dictated by the structural features at various length scales, as such, tremendous efforts in the past decades were dedicated to tailoring the chemical responses by doping,[3−5] controlling the morphologies,[6] tuning tortuosity,[7] and engineering the interfaces.[8−10] Defects are prevalent in electrochemical materials.[11,12] The subtle variation of the local chemical environment at the atomic scale can drastically alter the redox kinetics and cast heterogeneity across a wide range of time and length scales. Figure 1 illustrates material defects present at the atomic scale up to the cell and pack levels of LIBs. At the large-scale modules, manufacturing defects such as deflected anode and overweld joints can plague the cyclic reliability and even cause battery explosion.[13,14] At the smaller scales, in the layered-oxide cathode for instance, the structural defects are widely dispersed including the inter- and intragranular cracks in the secondary particles,[15−19] grain boundaries (GBs) between the primary particles,[20] dislocations inside the single-crystal domains,[21] and point defects such as vacancies, cation mixing, and lattice distortion at the nanoscale.[22,23] Material defects interact with the Li kinetics in a complex manner; on the one hand, they can aggravate the structural instability and cause progressive degradation of the cyclic performance, on the other hand, they may facilitate the kinetics of Li transport and charge transfer, and thus promising defect engineering of capacity and rate capability for battery materials.[24]

Grain boundaries are the nexus of multiscale defects and have evoked enormous interest in electrochemical materials due to their distinct physicochemical properties from the bulk, including the thermodynamic, transport,[25,26] electrochemical,[27] and mechanical[28] responses. However, it remains elusive how the GBs are intertwined with Li reaction kinetics in LIBs. In a prior study of the solid-state electrolyte $Li_{3x}La_{2/3-x}TiO_3$ (LLTO), it was found that GBs impeded Li-ion transport by the severe deformation of the Ti−O polyhedral and the

Received: March 17, 2021
Revised: April 28, 2021
Published: May 10, 2021

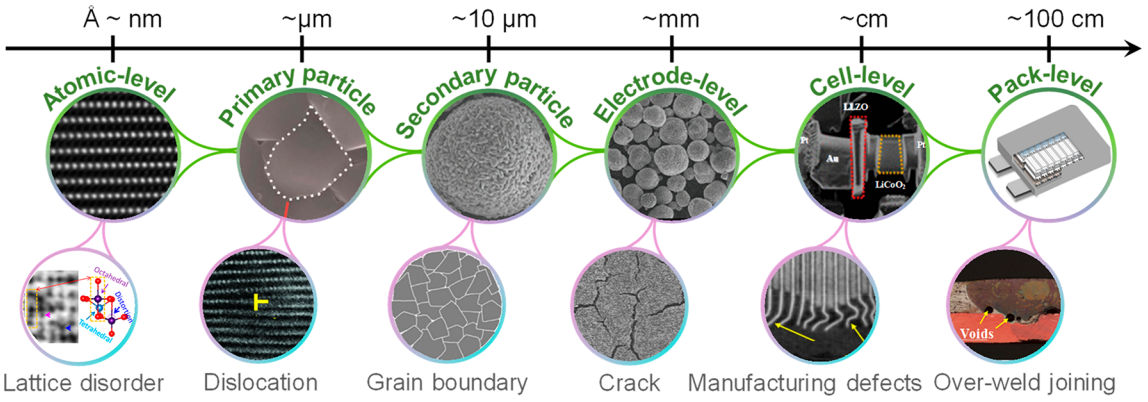

Figure 1. Defects in LIBs spanning multiple length scales from the atomic to the pack levels, including lattice disorder at a few angstroms or nanometers, dislocations at tens to hundreds of nanometers in the primary particles, grain boundaries at several micrometers in the secondary particles, cracks extending to tens of micrometers in the composite electrodes, and manufacturing defects such as deflected anode in the cells, and overweld joining in battery packs. Graphics reproduced from the references with permission: (Lattice disorder) ref 22. Copyright 2017 American Chemical Society. (Atomic-level) ref 42. Copyright 2020 Elsevier. (Dislocation) ref 21. Copyright 2017 Springer Nature. (Primary particle) ref 43. Copyright 2017 American Chemical Society. (Grain boundary) ref 20. Copyright 2018 Springer Nature. (Secondary particle) ref 40. Copyright 2019 John Wiley and Sons. (Crack) ref 16. Copyright 2018 IOP Publishing, Ltd. (Electrode-level) ref 40. Copyright 2019 John Wiley and Sons. (Manufacturing defects) ref 13. Copyright 2018 MDPI. (Cell-level) ref 44. Copyright 2017 American Chemical Society. (Over-weld joining) ref 14. Copyright 2014 Elsevier.

deviation of the chemical composition at the interfaces.[29,30] In contrast, the interconnected network of GBs in the $Li_4Ti_5O_{12}$ anode serves as the fast diffusion channel for Li atoms, thus enhancing the ionic conductivity and enabling fast charging performance.[31] In the SnO_2 anode, the twin boundaries (TBs), a special form of GBs, provide energetically favorable sites for Li intercalation and thus promote the capacity and assist with Li migration.[32] A few recent studies on GBs in layered-oxide cathode materials were reported. In $LiCoO_2$, a study performed by conductive atomic force microscopy (c-AFM) observed that GB planes generally acted as fast pathways for Li transport.[33] Atomistic modeling[34] further revealed that the coherent GBs/TBs in $LiCoO_2$ facilitated Li migration along the GB with 3 orders of magnitude higher diffusivity than that across the GB. Asymmetric GBs were found to significantly block Li transport across the grain planes.[35] Albeit $LiCoO_2$ has been widely used in portable devices since its commercialization in 1991, its major drawbacks are low practical capacity, high material cost, and the toxicity of cobalt.[36] The NMC family, with a general formula of $LiNi_{1-x-y}Mn_xCo_yO_2$, emerges as the state-of-the-art cathode of choice[37−39] that can deliver a higher specific capacity and lower cost than $LiCoO_2$. The defect chemistry in NMC is largely unexplored. More recently, Lee et al.[40] and Sharifi-Asl et al.[41] observed highly coherent symmetrical GBs in experiments; however, the impact of GBs on Li transport and its context on the rate performance in NMC are yet to be elaborated. It is an urgent task to understand the microstructures of GBs in NMC and their relationship to the capacity and reaction kinetics in LIBs, so that layered-oxide cathodes of enhanced rate capability and structural stability can be rationally designed.

In this paper, we use $LiNi_{0.5}Mn_{0.3}Co_{0.2}O_2$ (NMC532, hereinafter referred to as NMC) as a model compound to systematically study the atomic features of grain boundaries and their deterministic effect on Li transport using the first-principles theoretical approach. We construct four representative coincidence site lattices of $\sum 2(1\bar{1}0\bar{4})$, $\sum 3(\bar{1}10\bar{2})$, $\sum 5(1\bar{1}0\bar{1})$, and $\sum 9(\bar{1}10\bar{4})$ GBs. The supercell models enable the studies of Li diffusion in the bulk, across the GBs, and along the grain planes at the short (~3 Å) and intermediate (~15 Å) ranges. The GBs of different microstructures play distinct roles in regulating Li migration and therefore causing significantly different Li diffusivities and overall conductivities. The coherent $\sum 2$ GB accelerates Li transport, both along and across the grain planes, due to its unique structural feature where oxygen atoms of different charge environments are colocated in the vicinity of the GB. The more negative Bader charge and smaller Voronoi occupancy of oxygen near the transition state of Li collectively reduce the barrier for Li migration. In comparison, the $\sum 3$ GB presents an asymmetric feature in which the transition-metal (TM) slab and the Li slab share the oxygen atoms along the GB. Because the TM slab has a smaller space than the Li slab, the lattice mismatch results in a smaller free volume for Li diffusion which reduces Li diffusivity by nearly 7 orders of magnitude across the GB. For the $\sum 5$ and $\sum 9$ GBs, the thickness of the GBs increases because of the locally disordered lattice. The amorphous-like network near the GBs promotes Li transport owing to the loosely packed interface. These findings provide theoretical understanding of a prevalent material defect in the layered oxides cathode, and shed important insights on the local Li transport regulated by the various natures of GBs which further infers Li conduction in NMC beyond the atomic scale.

2. METHODS SECTION

Density functional theory (DFT) calculations and DFT-based ab initio molecular dynamics (AIMD) simulations are performed using the Vienna Ab initio Simulation Package (VASP).[45] The projector augmented wave (PAW) method[46] is implemented with a kinetic energy cutoff of 520 eV to describe the ion−electron interaction. The exchange and correlation energy functional Perdew-Burke-Ernzerh of generalized gradient approximation (GGA-PBE) is employed.[47] Due to the very large supercell (each supercell contains 240 atoms), the Brillouin zone is sampled by 3 × 1 × 1 *k*-points in the Monkhorst−Pack scheme for DFT computations, while single Γ point Brillouin zone sampling is applied for the AIMD simulations. Lattice constants and atomic coordinates are fully

https://doi.org/10.1021/acs.jpcc.1c02400
J. Phys. Chem. C 2021, 125, 10284−10294

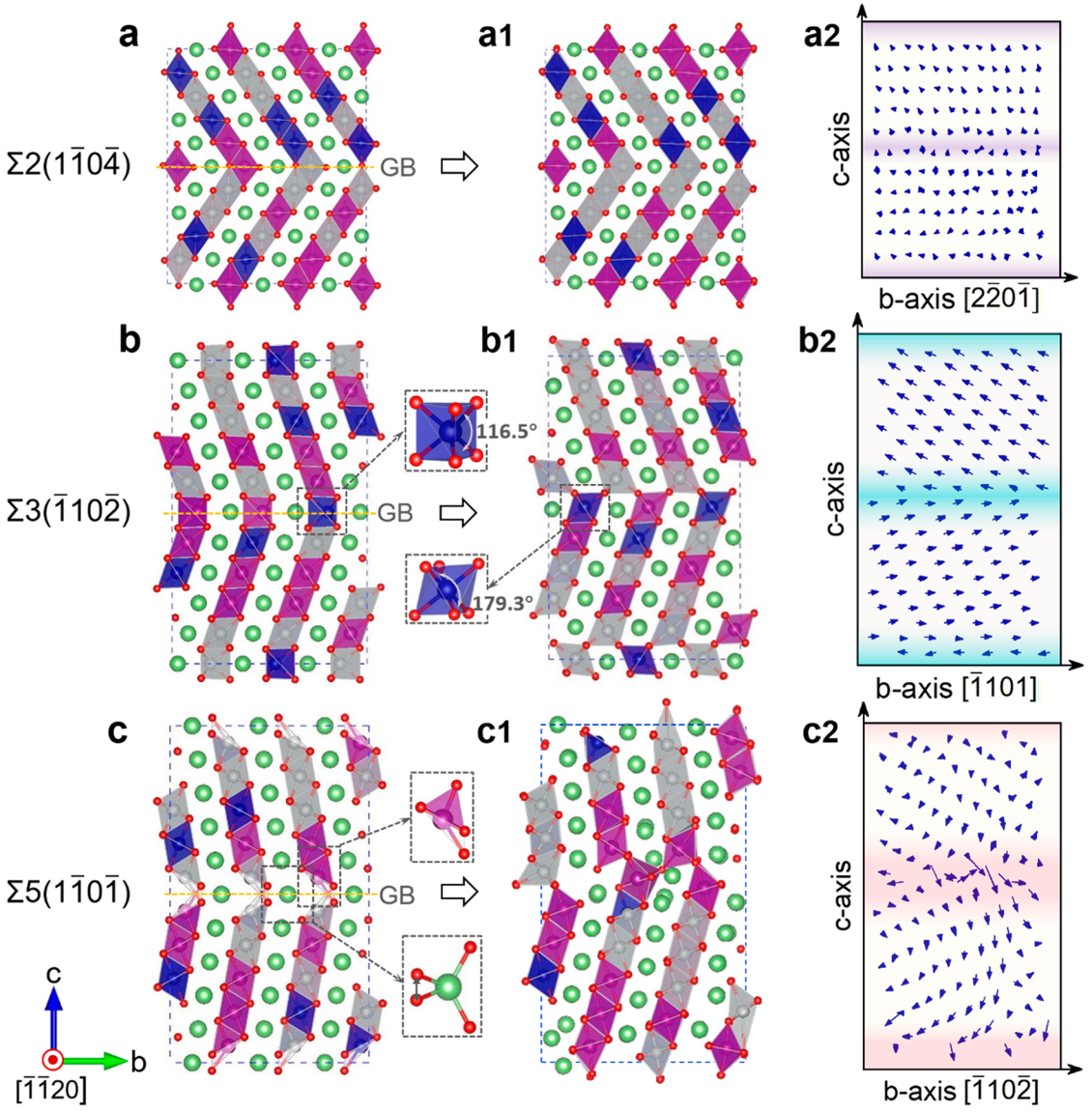

Figure 2. Atomic structures of NMC supercells of several representative GBs. (a,b,c) pristine bicrystalline NMC lattices with the grain boundary of $\sum$2(1$\bar{1}$04), $\sum$3($\bar{1}$10$\bar{2}$), and $\sum$5(1$\bar{1}$0$\bar{1}$), respectively. (a1−c1) GB structures after energy relaxation. Grains remain symmetric about the $\sum$2 GB (a1), grains become asymmetric about the $\sum$3 GB due to the translational motion of the GB in the *b*-axis direction (b1), and lattice is disordered nearby the $\sum$5 GB (c1). The distorted polyhedral units of TMO_6 and LiO_6 at the GBs are shown in the enlarged panels. (a2−c2) atomic displacement trajectories after the structural relaxation. The green, blue, gray, purple, and red spheres represent the Li, Co, Ni, Mn, and O atoms, respectively.

optimized with an energy convergence of 10^{-5} eV per atom and the force convergence of 0.04 eV $Å^{-1}$. The DFT+*U* method was used to treat the TM-3*d* states, combining van der Waals (vdW) corrections (DFT+D3) with DFT+*U* to yield structural properties of high accuracy compared to the experimental results.[48,49] Li diffusion barriers are calculated using the climbing image nudged elastic band (CI-NEB) calculations, which are complementary to the NEB method.[50,51] CI-NEB calculations are carried out with the standard PBE functional (without +*U*) to avoid the overlocalization of electron density between the diffusion barrier and the charge transfer barrier.[49,52−54] The lattice parameters for CI-NEB calculations are fixed, and are obtained from the PBE+*U*+D3 structural optimization processes. Dispersion corrections are negligible for the CI-NEB calculations since Li diffusion barriers are calculated at the fully lithiated state and with a fixed lattice parameter. Full details are given in the Supporting Information.

3. RESULTS AND DISCUSSION

GB Model Construction. We construct four symmetric tilt GB supercells (Figure S1, Supporting Information) with low-$\sum$ and low-index planes based on the coincidence site lattice (CSL) theory,[55] namely, $\sum$2(1$\bar{1}$04)[$\bar{1}$120], $\sum$3($\bar{1}$10$\bar{2}$)[$\bar{1}$120], $\sum$5(1$\bar{1}$0$\bar{1}$)[$\bar{1}$120] and $\sum$9($\bar{1}$10$\bar{4}$)[$\bar{1}$120], hereafter termed as $\sum$2, $\sum$3, $\sum$5, and $\sum$9 for short, respectively. It is worth noting that all the GB supercell models contain the energetically favorable TM configurations verified by the USPEX program.[56] We do not find TM clustering or ordering at the GB core which is a similar finding in our earlier work.[57] We also note that it is not possible to construct a $\sum$7 grain structure with a low-index crystal plane and a low GB energy in NMC. Two

https://doi.org/10.1021/acs.jpcc.1c02400
J. Phys. Chem. C 2021, 125, 10284−10294

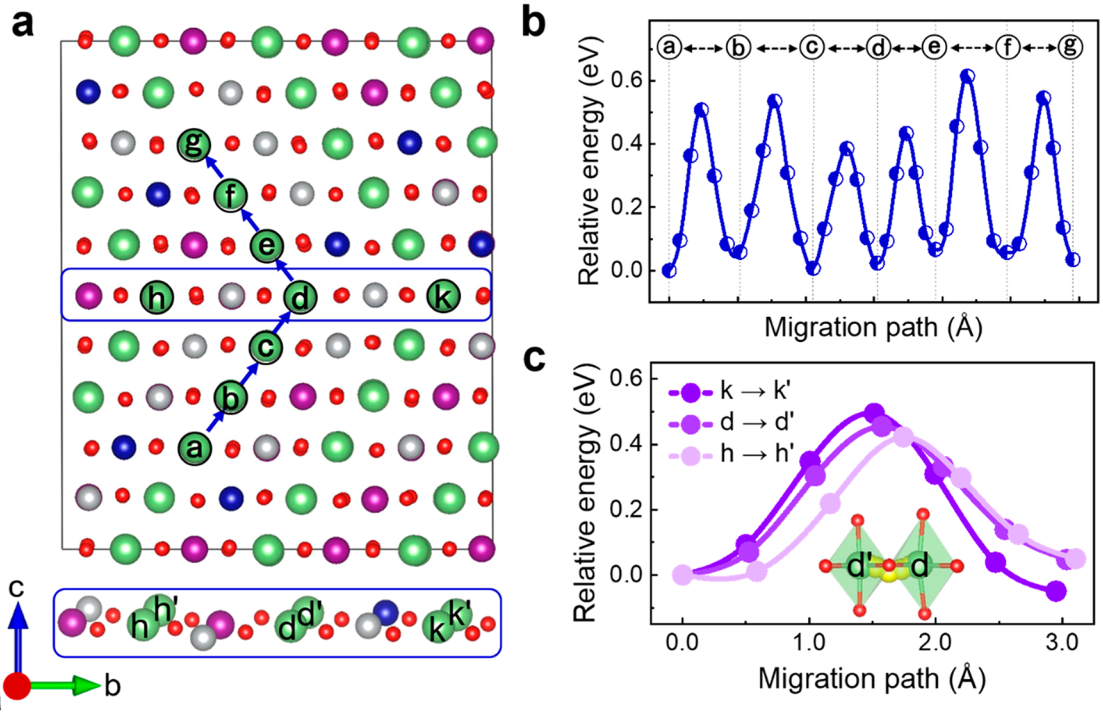

Figure 3. Li migration pathways across and along the ∑2 GB. (a) Li transport across the GB from the sites a to g, and within the GB plane from the sites h, d, k to h′, d′, and k′, respectively. The blue arrows indicate the migration direction of each substep. (b,c) energy profiles for Li transport across and within the ∑2 GB plane, respectively. Inset in panel c displays a typical octahedra−octahedra path for Li diffusion in the grain plane.

equivalent GBs are located at the center and the top/bottom of the bicrystalline supercells. The supercells contain 240 atoms. The model size is consciously relatively small for the exploration of grain boundaries with a wide range of perturbations of the equilibrium structures. Our choice of the supercells affords the explorations of Li transport at the intermediate diffusion distance at a reasonable balance of computational accuracy and cost. According to the CSL theory, grain boundaries can be built by either tilting the grains about a specific axis or twisting them against a special plane.[58] All the GB models in this work are generated by the tilting method, where the grains are rotated by specific angles about the tilt axis $[\bar{1}120]$ (see Table S1, Supporting Information).

Structural Optimization. To obtain the thermodynamically stable GB structures, we perform annealing at an elevated temperature and quenching using AIMD and subsequent geometric optimization using DFT modeling. This procedure and model parameters (Supporting Information) were calibrated by comparing the model GB configurations in $LiCoO_2$ obtained via the rigid body translation method.[34,35] Figure 2 shows three representative GBs and the displacement trajectories for all the atoms mapping from the pristine states to the energetically optimized structures. ∑2 GB retains its mirror symmetry (Figure 2a1) with a notably low GB energy (γ_{GB}) of 0.097 J m^{-2} (Figure S1). In comparison, GBs of higher ∑ values present distinct structural features compared with their initial states. The upper grain in the ∑3 model translates by 1.786 Å relative to the lower counterpart along the *b*-axis (Figure 2b1). The GB energy is calculated as 0.286 J m^{-2}. ∑5 exhibits slightly shifted grains as well as a disordered lattice surrounding the GB (Figure 2c1). The GB energy reaches 1.836 J m^{-2} which is significantly larger than that of the lower-∑ GBs. Similarly, the distorted lattice nearby the ∑9 GB leads to a high GB energy of 1.649 J m^{-2} (Figure S1). The energetic analysis suggests that the ∑2 and ∑3 GBs (especially ∑2) are more likely stabilized in NMC grains given their lower GB energies and less lattice distortion. This finding is consistent with the experimental results in which ∑2 GBs in $LiCoO_2$ are most observed.[34,44]

The translational motion in ∑3 GBs and the lattice distortion/amorphization of ∑5 GBs are attributed to their atomic features. In the pristine ∑3 GBs, the TMO_6 complex at the GB core presents a prismatic structure (Figure 2b), of which the O−TM−O dihedral angles are significantly distorted (~116.5°) compared to those of the regular TMO_6 octahedra (~179.3°). Nevertheless, the coordination number and the coordinating atoms of TMs and Li around the GB are not altered, thus the shear stress in the distorted TMO_6 polyhedra drives the formation of asymmetric ∑3 GBs as shown in Figure 2b1. For ∑5 GBs, in addition to the lattice distortion in the initially generated structure, O atoms around the GBs are in close proximity while Li atoms at the GBs are loosely packed, both of which disturb the lattice. Meanwhile, the effective coordination number and the coordinating species of TMs and Li near the GB are changed, which provides a large driving force to disorder the lattice around the GB (Figure 2c2). The blue arrows in Figure 2a2−c2 draw the displacement vectors of atoms from their original positions (Figure 2a-c) to the optimized positions (Figure 2a1−c1). The trend of the GB evolution with the increasing ∑ is clear−the atoms in the ∑2 model only vibrate locally around their original positions, the upper and lower grains of ∑3 slide against each other to mitigate the local shear stress, while the complex GB core structure of ∑5 distorts the surrounding atoms and leads to a turbulent flow in their displacement map.

In addition to the GB energy as discussed above, the GB structural stability can be quantitatively evaluated by the vacancy formation energy (or configurational energy) for the

https://doi.org/10.1021/acs.jpcc.1c02400
J. Phys. Chem. C 2021, 125, 10284−10294

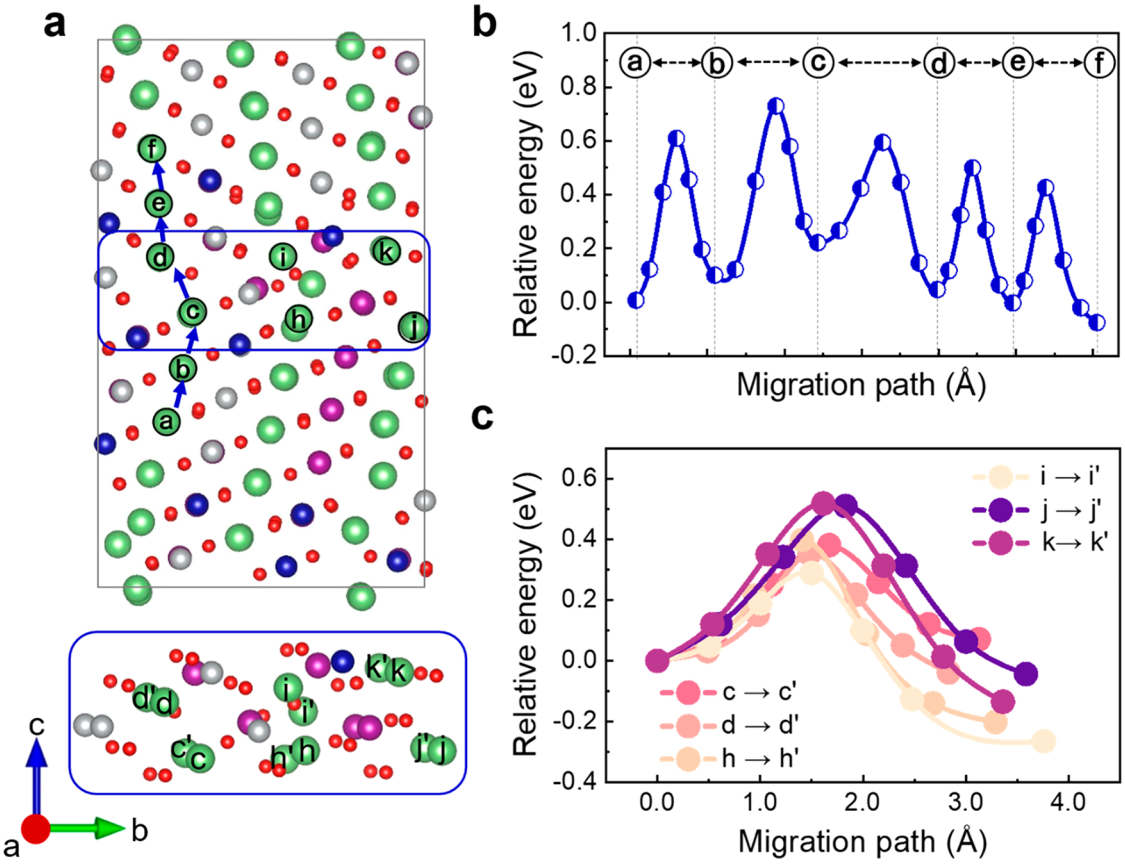

Figure 4. Energy profiles for Li hopping in the vicinity of the disordered ∑5 GB. (a) Li diffusion across (from site a to f) and within (c–c′, d–d′, h–h′, i–i′, j–j′, and k–k′) the GB plane. (b) The energy profiles along the Li migration pathway across the GB. (c) The energy barriers with a large variation for Li diffusion within the GB plane.

structures containing different Li-vacancy populations at the GB.[4,59] More generally, this method can be used to determine the structural stability of the NMC lattice as a function of the Li concentration upon Li deintercalation. Herein, as we focus on the pristine state in which the Li sites are fully occupied, Li diffusion is primarily dominated by the oxygen dumbbell hopping (ODH) mechanism, which is also referred to as isolated-vacancy diffusion.[60] The formation energy $E_{\text{Formation}}$ is defined as[59]

$$E_{\text{Formation}} = E(\text{Li}_{1-x}\text{MO}_2) - (1-x)E(\text{LiMO}_2) - xE(\text{MO}_2) \quad (1)$$

where M = $Ni_{0.5}Mn_{0.3}Co_{0.2}$, x = 0.0167 for a single vacancy in the supercell containing 60 Li atoms, $E(\text{Li}_{1-x}\text{MO}_2)$ is the total energy of the GB model with 1.67% of Li-vacancies, $E(\text{LiMO}_2)$ and $E(\text{MO}_2)$ are the free energies of the fully lithiated and the fully delithiated states, respectively. A lower value (more negative) of E_{form} represents a higher structural stability upon Li extraction. Figure S2 shows the Li-vacancy formation energy (E_{form}) as a function of the ∑ value. To minimize the variation inherent to the small model size, we consider four possible configurations of $\text{Li}_{1-x}\text{MO}_2$ of the same Li concentration in our calculations. The open squares in Figure S2 represent the average values of the vacancy formation energy and the error bars are the standard deviation. The results show that E_{form} for all the GB models are negative, confirming the structural stability of the NMC lattice for Li migration mediated by the vacancy mechanism.

Li Transport Characterization. We next explore the kinetics of Li transport in the NMC lattice of various GB structures. We determine the activation energies of Li migration in the bulk, along the grain planes, and across the GBs separately, and then evaluate the overall Li diffusivity and conductivity in the NMC electrode. We employ the CI-NEB method to obtain the optimized Li migration pathways and calculate the energy barriers at the transient state.[50,51] Taking the single crystal NMC as a reference structure (see Figure S3), the energy barrier of Li diffusion is determined as E_{ave} = 0.505 eV, being consistent with the result of a prior report.[49] The lattice parameters a = 2.908 Å and c = 14.220 Å are also found in excellent agreement with the experimental results.[61,62]

To examine the influence of GBs on Li transport, we investigate four representative types of GB models from the ∑2 GB of a high mirror symmetry to the ∑9 GB of a much-reduced symmetry. Each model is divided into the GB region and the bulk-like grain region. Near the GBs, Li migration can be classified into two types: one is across the GB plane (⊥) and the other along the GB plane (//). Li diffusion within the bulk grain, across the GB planes, and along the GBs are simulated separately, with their energy barriers denoted as E_{bulk}, $E_{\text{GB}\perp}$, and $E_{\text{GB}//}$, respectively. For the coherent ∑2 GB, Figure 3a shows Li diffusion pathways across the GB plane labeled as a-b-c-d-e-f-g, and along the GB marked as h-h′, d-d′, and k-k′. Figure 3b and Figure 3c plot their corresponding energy profiles. The energy barrier of Li diffusion across the GB (from the sites c to d and then d to e) possesses a notably lower value of $E_{\text{GB}\perp\text{-}\sum 2}$ = 0.389 eV compared with that of Li

https://doi.org/10.1021/acs.jpcc.1c02400
J. Phys. Chem. C 2021, 125, 10284−10294

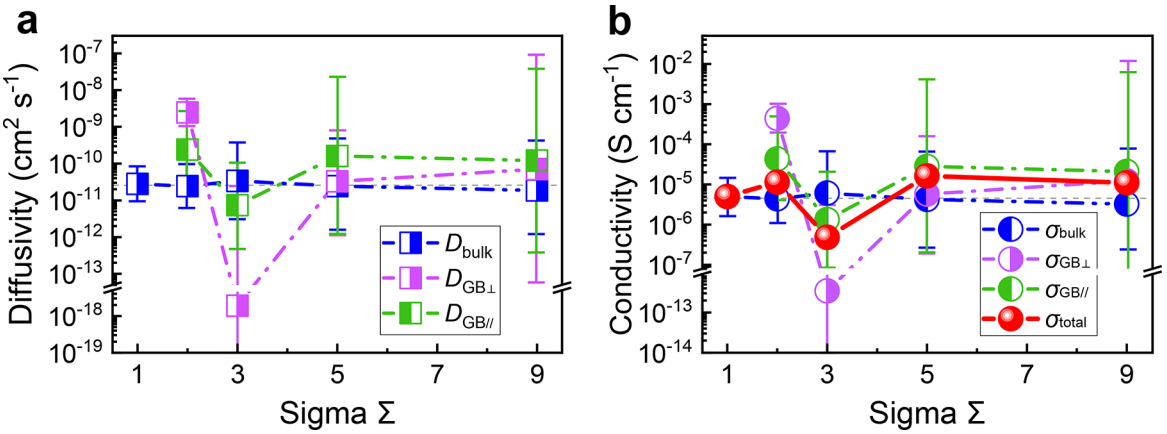

Figure 5. GB contributions to Li diffusivity and Li conductivity in NMC at T = 300 K. (a) Li diffusivities in the bulk-like grains (D_{bulk}, blue squares), across ($D_{GB⊥}$, purple squares), and along ($D_{GB//}$, green squares) the GB plane in the supercells. (b) Li conductivities in the bulk-like grains (σ_{bulk}, blue circles), across the GB plane ($\sigma_{GB⊥}$, purple circles), along the GB plane ($\sigma_{GB//}$, green circles) and the effective conductivity (σ_{total}, red points) of the supercell as a function of the ∑ values. Error bars represent the standard deviation.

migration in the bulk lattice (from the sites a to c and e to g) which has an average value of $E_{bulk\text{-}\sum 2}$ = 0.508 eV. Likewise, the energy barrier of Li migration along the GB plane, $E_{GB//\text{-}\sum 2}$ = 0.449 eV, is also smaller than that of bulk diffusion. Besides, no obvious vacancy segregation is observed at the GB; for instance, there is nearly no difference in the vacancy energy between the sites b, d, and c in Figure 3b which implies that Li trapping at the GB is less likely. This result demonstrates that the ∑2 GB facilitates Li transport in NMC by acting as a fast channel for Li conduction. The mechanistic understanding in terms of the charge environment and the local atomic features will be discussed later altogether with other types of GBs.

In the asymmetric ∑3 model, the Li diffusion pathways and the corresponding energy profiles are shown in Figure S4. The average energy barrier of Li across the translational GB plane from the sites b to e is calculated as 0.931 eV, which is significantly higher than that of bulk diffusion with $E_{bulk\text{-}\sum 3}$ = 0.501 eV (Figure S4b). Such a high activation barrier will block Li migration across the GB plane. For the diffusion within the GB plane, the energy profiles are relatively uniform, and the average energy barrier is $E_{GB//\text{-}\sum 3}$ = 0.539 eV (Figure S4c). The extremely high energy barriers for Li migration across the GB and the increased cost along the grain plane demonstrate the unfavored Li transport in the NMC lattices containing asymmetric ∑3 GBs. Specifically, compared to the positive effect of ∑2 GBs shown in Figure 3, ∑3 GBs perform as nearly a dead-end for Li transport across them. The distinct effects are due to the local coordination surrounding Li and the charge redistribution which will be rationalized in a later section.

The drastically different behaviors of ∑2 and ∑3 are evidence of the complex effect of GB structures on the Li kinetics for battery materials. To continue the survey of different types of GBs, we construct GBs of higher ∑ values to understand the impact on Li transport by the local amorphous network. The diffusion trajectories and the energy barriers for Li migration in the vicinity of the distorted ∑5 GB are shown in Figure 4. The oblique GB pathway is marked by b−e in Figure 4a, and the corresponding energy profile is shown in Figure 4b. The overall barrier across the grain plane, $E_{GB⊥\text{-}\sum 5}$ = 0.499 eV, is about the same as that of bulk diffusion $E_{bulk\text{-}\sum 5}$ = 0.508 eV (calculated by the substeps of a−b and e−f in Figure 4a). It should be noted that the local environment for Li in ∑5 varies substantially around the GB. To minimize the error due to the limited sampling paths, we calculate the energy profiles for Li diffusion in all parallel pathways within the GB plane as denoted by the lower panel in Figure 4a. The energy barriers are in the range from 0.288 to 0.653 eV (Figure 4c) with the mean value of $E_{GB//\text{-}\sum 5}$ = 0.459 eV. The result shows a locally anisotropic transport behavior of Li in ∑5, and in general, that the amorphous-like GB increases the rate of Li migration due to the loosely packed interface.

A similar study on the ∑9 GB is performed with two prospective Li diffusion paths perpendicular to the GB being identified, which are labeled as a1−a6 and b1−b6 in Figure S5. Along the path a, the sites a3 and a4 near the GB are the energetically favorable positions with a negative Li segregation energy of −0.45 eV, and the energy barrier between a3 and a4 is rather small at around ∼0.2 eV. For the path b, the GB effect is not as substantial as for path a. The average barrier for Li across the GB (substeps a2−a5 and b2−b4), $E_{GB⊥\text{-}\sum 9}$ = 0.481 eV, is slightly smaller than its diffusion in the bulk regime. The overall results of ∑5 and ∑9 GBs indicate facile Li migration mediated by the distorted lattice around the high-∑ GBs.

Evaluation of Li Kinetics. Now we can use the calculated energy barriers to determine the Li diffusivity (D) in various GB structures. The diffusivity is determined by the rate of Li migration through the host, and the hopping rate Γ can be approximated by the transition state theory[63]

$$\Gamma(T) = \nu^* \exp\left(\frac{-\Delta G}{k_B T}\right) \quad (2)$$

where ν^* is the effective vibration frequency for which 10^{11} to 10^{13} s^{-1} are the typical values.[64,65] Here we choose 10^{13} s^{-1} as an approximation in our calculations.[66] The activation energy $\Delta G \approx E_a$, where E_a is the above calculated barriers E_{bulk}, $E_{GB⊥}$, and $E_{GB//}$; k_B is the Boltzmann constant; and T = 300 K is the temperature. The diffusivity is then determined by $D(T) = d^2\Gamma(T)$, where d is the hopping distance which is roughly estimated by the lattice parameter in the a-axis direction in each GB system.[67]

We can convert the diffusivity D to Li conductivity σ via the following Nernst−Einstein relationship to compare with the experimental measurement:

https://doi.org/10.1021/acs.jpcc.1c02400
J. Phys. Chem. C 2021, 125, 10284−10294

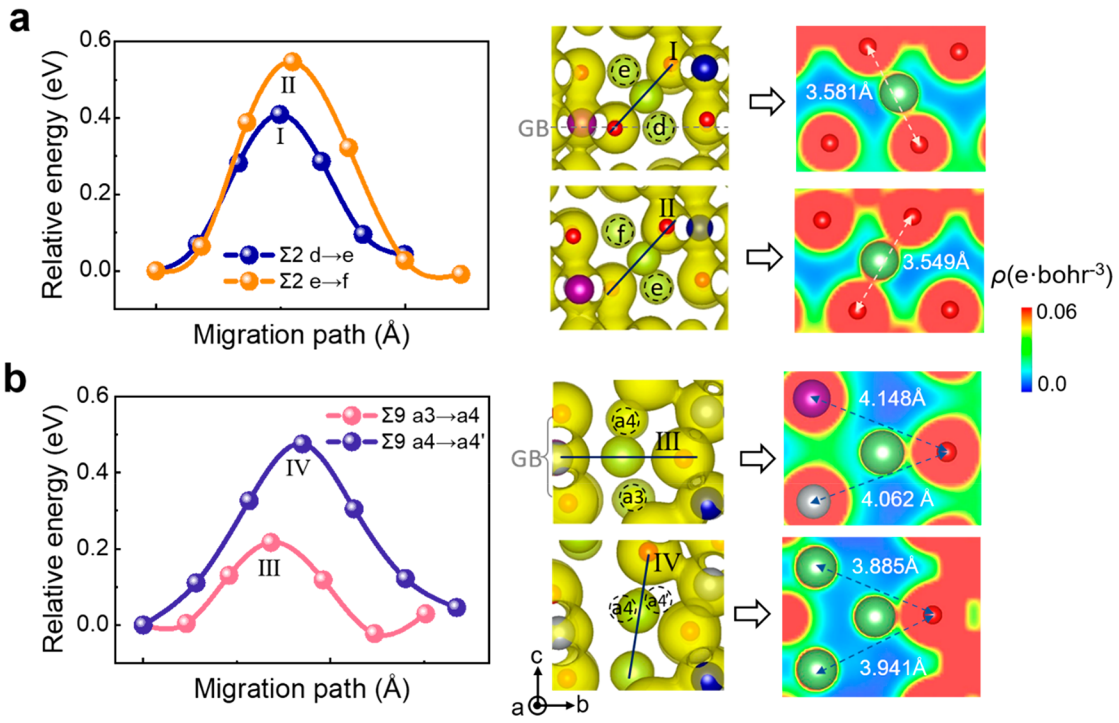

Figure 6. Isosurfaces of charge density distributions at the transition states of Li migration. The transition states are labeled as I and II for the coherent symmetric GB ∑2 in (a) and as III and IV for the disordered ∑9 GB in (b). 2D projections of the charge density distribution at the transition states (the third column) are viewed along the specific cut planes (black lines) in the 3D space (the second column).

$$\sigma(T) = \frac{N_{Li}q^2}{Vk_BT}D(T) \tag{3}$$

where N_{Li} is the number of Li atoms (or charge carriers) by assuming that all the Li atoms are the charge carrier of conductivity, V is the supercell volume, and q is the electronic charge. To rationalize the GB effect on the overall conductivity for each polycrystalline system, the total conductivity σ_{total} is introduced. σ_{total} is an effective value by combining the contributions of the bulk and the GB conductivities. It is evaluated according to a generalized equivalent circuit model[68] which is expressed as[69]

$$\sigma_{total} = \varphi_{bulk}\left(\frac{1}{\sigma_{bulk}} + \frac{l_{GB}}{d}\frac{1}{\sigma_{GB\perp}}\right)^{-1} + \varphi_{GB}\sigma_{GB//} \tag{4}$$

where σ_{total}, σ_{bulk}, $\sigma_{GB\perp}$, and $\sigma_{GB//}$ are the total conductivity, the bulk conductivity, and the GB conductivities across and along the GB plane, respectively. φ_{bulk} and φ_{GB} respresent the volume fraction of the bulk-like grain and the GB regime, respectively. l_{GB} is the thickness of the GB, and d is the grain size.

Figure 5 displays the variation of Li diffusivities and conductivities in the various GB structures at T = 300 K. As discussed above, we distinguish the bulk diffusion, across and along the GB plane transport, and denote the diffusivities by D_{bulk}, $D_{GB\perp}$, and $D_{GB//}$, and conductivities by σ_{bulk}, $\sigma_{GB\perp}$, and $\sigma_{GB//}$, respectively. The symbols in Figure 5 represent the average values calculated by different pathways as specified before for each ∑ system, and the error bars are the standard deviation. In Figure 5a, the bulk diffusivity for the GB structures (blue squares) remains approximately a constant of $D_{bulk} = 2.5 \times 10^{-11}$ cm^2 s^{-1}, which agrees very well with the experimental values of 4.64×10^{-11} cm^2 s^{-1}[70] and 1.55×10^{-12} cm^2 s^{-1}.[62] Diffusivities across and along the GB plane vary substantially depending on the nature of the GBs. $D_{GB//}$ and $D_{GB\perp}$ in ∑2 are 1−2 orders of magnitude larger than D_{bulk}, while $D_{GB//}$ and $D_{GB\perp}$ in ∑3 are smaller than D_{bulk} by 4 times and 7 orders of magnitude, respectively. For ∑5 and ∑9, the overall diffusivities of $D_{GB\perp}$ and $D_{GB//}$ are 1−10 times higher than that of bulk diffusivity with a large error bar. Using the Nernst−Einstein relationship, Li conductivity is shown in Figure 5b. Li conductivity in the perfect single crystal NMC, σ = 4.99×10^{-6} S cm^{-1}, again agrees well with the previous study.[62] The variation of the conductivity with an increased ∑ follows the same trend as the diffusivity (Figure 5b). Compared to the single crystal, the total conductivity σ_{total} for ∑2 is ∼2.3 times (1.14×10^{-5} S cm^{-1}) higher, whereas ∑3 reduces σ_{total} by 1 order of magnitude (4.83×10^{-7} S cm^{-1}). σ_{total} for ∑5 and ∑9 are around 2−3 times higher than that for the single crystals. Clearly, both the Li diffusivity and conductivity are dependent on the specific GB structures; meanwhile, it is noteworthy that the effective conductivity σ_{total} does not change drastically due to the relatively small fraction of the GBs.

Local Atomic Environment Analysis. The local atomic environment and charge interactions are responsible for the distinct Li transport behaviors in different GB models. To understand the underlying mechanism, we analyze the Li occupation volume, distortion of the Li−O polyhedral, and Bader charges for the GBs before Li migrates, and charge density redistribution at the transient state of Li migration. The local microstructural features surrounding Li atoms are quantitatively represented by the Voronoi volume of Li atoms (V_{Li}) and the local distortion index of Li-polyhedra. We introduce the distortion index (d_{Li}) as follows:

$$d_{Li} = \frac{1}{n}\sum_{i=1}^{n}\left(\frac{|\theta_i - \theta_{ave}|}{\theta_{ave}}\right) \tag{5}$$

https://doi.org/10.1021/acs.jpcc.1c02400
J. Phys. Chem. C 2021, 125, 10284−10294

where θ_i is the O−Li−O dihedral angle for the central Li with the i^{th} pair of the two neighboring O atoms, $\theta_{ave} = 90°$ is the average O−Li−O angle in the regular LiO_6 octahedra. The variation of the averaged V_{Li} and d_{Li} along the *c*-axis (i.e., GB−bulk−GB−bulk−GB) is shown in Figure S6. For the $\sum 2$ GBs, both V_{Li} and d_{Li} remain nearly a constant in the supercell. In contrast, V_{Li} and d_{Li} in $\sum 3$, $\sum 5$, and $\sum 9$ models show distinct values at the GB regions versus in the bulk-like grains. More specifically, $\sum 3$ exhibits a smaller V_{Li} and a larger d_{Li} at the GB compared to its bulk counterpart due to the lattice mismatch between the TM slab (space distance 2.17 Å) and the Li slab (space distance 2.58 Å) at the GB, which leads to the reduced Li occupation volume and increased structural distortion (Figure S7b). The GB regions in $\sum 5$ and $\sum 9$ GB show larger values of V_{Li} and d_{Li} due to the under-coordinated Li atoms, causing loosely packed GB structures and locally disordered lattices. In general, a larger Voronoi volume of Li would facilitate Li diffusion with a reduced energy barrier. However, the high local distortion of the Li-polyhedra in the course of Li diffusion can induce a competing effect. On the one hand, the lattice distortion may reduce the coordination number of Li, and thus facilitate Li migration, on the other hand, some residing atoms close to Li (i.e., O atoms in $\sum 5$ and $\sum 9$ GBs) would hinder Li transport. The analyses of the Voronoi volume and the distortion index of Li polyhedra is inadequate to fully describe the local chemistry of Li atoms in the $\sum 2$ GB because of its coherent structure. The coordination environment of two O sites at the GB is different from that in the bulk. In the arrow direction of the GB (Figure S7a), at the odd number sites, O atoms (Type1) are coordinated by 4 Li atoms and 2 TM atoms (4Li+2TM), while at the even number sites, O atoms (Type2) are coordinated by 2Li+4TM. In contrast, O atoms (Type3) in the bulk are bonded by 3Li+3TM. In the pristine NMC, the average Bader charge of the above three types of O atoms is −1.1872 *e*, −1.0935 *e*, and −1.1329 *e*, respectively. The Type1 O atoms play a larger role in Li migration compared to Tpye2, because Type1 O is much closer to the transition state, as shown in the substep path c−d in Figure S7a. The more negative Bader charge of Type1 O provides a stronger attraction force for Li migration to the transition state. Furthermore, the smaller Voronoi occupation of Type1 O atoms also supplies a larger space for the Li passage. The distinct O coordination at the GB explains the lower energy barrier for Li migration across and along the $\sum 2$ GB relative to the bulk behavior.

To summarize and provide an intuition on the relationship between the diffusion energy barrier and the local configurations, Figure 6 shows the charge density redistribution at the transition state, wherein the charge accumulation/depletion serves as an indicator of the strengthening/weakening of the interatomic bonding. Two types of the GB structures and their representative subtrajectories are shown, one is the coherent $\sum 2$ GB (Figure 6a) and the other is the disordered $\sum 9$ GB (Figure 6b). At the transition state, the diagonal space between O atoms at the state II (3.549 Å) is shorter than that of the state I (3.581 Å), which indicates a smaller free volume of Li and a stronger charge interaction between Li and O at the state II. As a result, the cost of Li passing the substep e−f (state II) is higher than that along d−e (state I). Likewise, the lower barrier of the substep a3−a4 in Figure 6b at the state III shows a weaker Li−O coupling relative to the state IV due to the larger interval distance of TM-O (4.105 Å). Albeit the different local bonding environments of Li at the transition states, such as the O−O interval for the cases I and II, TM−O interval for the case III, and Li−O interval for the case IV, a general observation is that the lower energy barrier is attributed to the relative larger interval space and the weaker Li−O/TM coupling for Li transport. To the end, the results reveal that the energy profile along Li migration is directly correlated with the Li space at the transition state, which as a whole is determined by the local microstructural features including the Li Voronoi volume, Li-polyhedral distortion, and the charge interactions with the neighboring atoms.

4. CONCLUSIONS

In summary, we study the grain boundaries in the layered-oxide cathode for Li-ion batteries and evaluate their impact on the Li transport kinetics at the intermediate diffusion length. We construct the representative supercells including $\sum 2(1\bar{1}04)[\bar{1}\bar{1}20]$, $\sum 3(\bar{1}10\bar{2})[\bar{1}\bar{1}20]$, $\sum 5(1\bar{1}0\bar{1})[\bar{1}\bar{1}20]$, and $\sum 9(\bar{1}\bar{1}04)[\bar{1}\bar{1}20]$ GBs of distinct atomic features. We use first-principles theoretical modeling to determine the thermodynamics and structural stabilities of the GBs, and then examine the energy profiles of Li transport in the bulk, across the GBs, and along the grain planes with a statistical evaluation. The energy barriers that Li needs to overcome at the transition states depend on the nature of the GBs but can be understood by the local space of Li migration. More detailed analysis on the Li Voronoi volume, Li-polyhedral distortion, and the Li−O/TM charge interactions and their contributions to the Li kinetics are elaborated. The specific conclusions are as follows: (i) the coherent $\sum 2$ GB exhibits the lowest GB energy of 0.097 J m^{-2} and enhanced Li transport both along and across the GB plane with 1−2 orders of magnitude increased diffusivity than that in the bulk, (ii) The asymmetric $\sum 3$ GB is formed by the translational motion of the bicrystalline grains and of a low GB boundary energy of 0.286 J m^{-2}. The $\sum 3$ GB significantly impedes Li transport with a reduced diffusivity by 7 orders of magnitude across the GB, (iii) The $\sum 5$ and $\sum 9$ GBs are of high GB energies and a disordered interface with increased thickness. The amorphous network generally promotes Li transport with an increased diffusivity up to 10 times that of the bulk diffusion; however, the large variation inherent to the small model size cannot be overlooked. (iv) We evaluate the effective conductivity of the polycrystalline NMC containing GBs which is found in a relatively narrow range of 2 orders of magnitude. This work addresses an important material defect in the layered-oxide cathode, and the findings are applicable for other compositions of NMC materials. The in-depth understanding of GBs/interfaces and their effects on Li kinetics is crucial for tailoring and designing polycrystalline cathodes of enhanced rate performance and structural reliability.

■ ASSOCIATED CONTENT

Supporting Information

The Supporting Information is available free of charge at https://pubs.acs.org/doi/10.1021/acs.jpcc.1c02400.

More details of computational methods; GB supercell models and the optimized structures; GB energies; structural stability analysis; Li migration pathways and energy barriers in the bulk, across and along $\sum 3$ and $\sum 9$ GBs; Voronoi volume of Li and local distortion of Li-

https://doi.org/10.1021/acs.jpcc.1c02400
J. Phys. Chem. C 2021, 125, 10284−10294

polyhedra; configurational features of ∑2 and ∑3 GBs (PDF)

AUTHOR INFORMATION

Corresponding Authors

Xiangdong Ding − *State Key Laboratory for Mechanical Behavior of Materials, Xi'an Jiaotong University, Xi'an 710049, China*; Email: dingxd@mail.xjtu.edu.cn

Kejie Zhao − *School of Mechanical Engineering, Purdue University, West Lafayette, Indiana 47907, United States*; orcid.org/0000-0001-5030-7412; Email: kjzhao@purdue.edu

Authors

Xiaomei He − *State Key Laboratory for Mechanical Behavior of Materials, Xi'an Jiaotong University, Xi'an 710049, China; School of Mechanical Engineering, Purdue University, West Lafayette, Indiana 47907, United States*

Hong Sun − *School of Mechanical Engineering, Purdue University, West Lafayette, Indiana 47907, United States*; orcid.org/0000-0002-3586-7400

Complete contact information is available at: https://pubs.acs.org/10.1021/acs.jpcc.1c02400

Notes

The authors declare no competing financial interest.

ACKNOWLEDGMENTS

X.H. acknowledges the support from Chinese Scholarship Council (No. 201906280164) for a visiting scholarship at Purdue University. H.S. and K.Z. are grateful for the support of the National Science Foundation through the Grants CMMI-1726392 and DMR-1832707.

REFERENCES

(1) Armand, M.; Tarascon, J.-M. Building Better Batteries. *Nature* **2008**, *451*, 652−657.

(2) Manthiram, A. An Outlook on Lithium Ion Battery Technology. *ACS Cent. Sci.* **2017**, *3*, 1063−1069.

(3) Schipper, F.; Bouzaglo, H.; Dixit, M.; Erickson, E. M.; Weigel, T.; Talianker, M.; Grinblat, J.; Burstein, L.; Schmidt, M.; Lampert, J.; et al. From Surface ZrO_2 Coating to Bulk Zr Doping by High Temperature Annealing of Nickel-Rich Lithiated Oxides and Their Enhanced Electrochemical Performance in Lithium Ion Batteries. *Adv. Energy Mater.* **2018**, *8*, 1701682.

(4) Dianat, A.; Seriani, N.; Bobeth, M.; Cuniberti, G. Effects of Al-Doping on the Properties of Li−Mn−Ni−O Cathode Materials for Li-Ion Batteries: An Ab Initio Study. *J. Mater. Chem. A* **2013**, *1*, 9273−9280.

(5) Liu, D.; Liu, S.; Zhang, C.; You, L.; Huang, T.; Yu, A. Revealing the Effect of Ti Doping on Significantly Enhancing Cyclic Performance at a High Cutoff Voltage for Ni-Rich $LiNi_{0.8}Co_{0.15}Al_{0.05}O_2$ Cathode. *ACS Sustainable Chem. Eng.* **2019**, *7*, 10661−10669.

(6) Lewis, J. A.; Cortes, F. J. Q.; Boebinger, M. G.; Tippens, J.; Marchese, T. S.; Kondekar, N.; Liu, X.; Chi, M.; McDowell, M. T. Interphase Morphology between a Solid-State Electrolyte and Lithium Controls Cell Failure. *ACS Energy Lett.* **2019**, *4*, 591−599.

(7) Ebner, M.; Chung, D.-W.; García, R. E.; Wood, V. Tortuosity Anisotropy in Lithium-Ion Battery Electrodes. *Adv. Energy Mater.* **2014**, *4*, 1301278.

(8) Haruyama, J.; Sodeyama, K.; Han, L.; Takada, K.; Tateyama, Y. Space−Charge Layer Effect at Interface between Oxide Cathode and Sulfide Electrolyte in All-Solid-State Lithium-Ion Battery. *Chem. Mater.* **2014**, *26*, 4248−4255.

(9) Edström, K.; Gustafsson, T.; Thomas, J. O. The Cathode−Electrolyte Interface in the Li-Ion Battery. *Electrochim. Acta* **2004**, *50*, 397−403.

(10) Lin, F.; Markus, I. M.; Nordlund, D.; Weng, T.-C.; Asta, M. D.; Xin, H. L.; Doeff, M. M. Surface Reconstruction and Chemical Evolution of Stoichiometric Layered Cathode Materials for Lithium-Ion Batteries. *Nat. Commun.* **2014**, *5*, 3529.

(11) Banhart, F.; Kotakoski, J.; Krasheninnikov, A. V. Structural Defects in Graphene. *ACS Nano* **2011**, *5*, 26−41.

(12) Xu, Z.; Hou, D.; Kautz, D. J.; Liu, W.; Xu, R.; Xiao, X.; Lin, F. Charging Reactions Promoted by Geometrically Necessary Dislocations in Battery Materials Revealed by In Situ Single-Particle Synchrotron Measurements. *Adv. Mater.* **2020**, *32*, 2003417.

(13) Wu, Y.; Saxena, S.; Xing, Y.; Wang, Y.; Li, C.; Yung, W. K.; Pecht, M. Analysis of Manufacturing-Induced Defects and Structural Deformations in Lithium-Ion Batteries Using Computed Tomography. *Energies* **2018**, *11*, 925.

(14) Solchenbach, T.; Plapper, P.; Cai, W. Electrical Performance of Laser Braze-Welded Aluminum−Copper Interconnects. *J. Manuf. Process.* **2014**, *16*, 183−189.

(15) Ryu, H.-H.; Park, K.-J.; Yoon, C. S.; Sun, Y.-K. Capacity Fading of Ni-Rich Li $[Ni_xCo_yMn_{1-x-y}]O_2$ ($0.6 \leq X \leq 0.95$) Cathodes for High-Energy-Density Lithium-Ion Batteries: Bulk or Surface Degradation? *Chem. Mater.* **2018**, *30*, 1155−1163.

(16) Lee, B.-S.; Wu, Z.; Petrova, V.; Xing, X.; Lim, H.-D.; Liu, H.; Liu, P. Analysis of Rate-Limiting Factors in Thick Electrodes for Electric Vehicle Applications. *J. Electrochem. Soc.* **2018**, *165*, A525−A533.

(17) Xu, R.; Yang, Y.; Yin, F.; Liu, P.; Cloetens, P.; Liu, Y.; Lin, F.; Zhao, K. Heterogeneous Damage in Li-Ion Batteries: Experimental Analysis and Theoretical Modeling. *J. Mech. Phys. Solids* **2019**, *129*, 160−183.

(18) Kim, U.-H.; Park, G.-T.; Son, B.-K.; Nam, G. W.; Liu, J.; Kuo, L.-Y.; Kaghazchi, P.; Yoon, C. S.; Sun, Y.-K. Heuristic Solution for Achieving Long-Term Cycle Stability for Ni-Rich Layered Cathodes at Full Depth of Discharge. *Nat. Energy* **2020**, *5*, 860−869.

(19) Yan, P.; Zheng, J.; Chen, T.; Luo, L.; Jiang, Y.; Wang, K.; Sui, M.; Zhang, J.-G.; Zhang, S.; Wang, C. Coupling of Electrochemically Triggered Thermal and Mechanical Effects to Aggravate Failure in a Layered Cathode. *Nat. Commun.* **2018**, *9*, 2437.

(20) Xu, R.; De Vasconcelos, L. S.; Shi, J.; Li, J.; Zhao, K. Disintegration of Meatball Electrodes for $LiNi_xMn_yCo_zO_2$ Cathode Materials. *Exp. Mech.* **2018**, *58*, 549−559.

(21) Yan, P.; Zheng, J.; Gu, M.; Xiao, J.; Zhang, J.-G.; Wang, C.-M. Intragranular Cracking as a Critical Barrier for High-Voltage Usage of Layer-Structured Cathode for Lithium-Ion Batteries. *Nat. Commun.* **2017**, *8*, 14101.

(22) Yan, P.; Zheng, J.; Zhang, J.-G.; Wang, C. Atomic Resolution Structural and Chemical Imaging Revealing the Sequential Migration of Ni, Co, and Mn upon the Battery Cycling of Layered Cathode. *Nano Lett.* **2017**, *17*, 3946−3951.

(23) Nakamura, T.; Gao, H.; Ohta, K.; Kimura, Y.; Tamenori, Y.; Nitta, K.; Ina, T.; Oishi, M.; Amezawa, K. Defect Chemical Studies on Oxygen Release from the Li-Rich Cathode Material $Li_{1.2}Mn_{0.6}Ni_{0.2}O_{2-\delta}$. *J. Mater. Chem. A* **2019**, *7*, 5009−5019.

(24) Zhang, Y.; Tao, L.; Xie, C.; Wang, D.; Zou, Y.; Chen, R.; Wang, Y.; Jia, C.; Wang, S. Defect Engineering on Electrode Materials for Rechargeable Batteries. *Adv. Mater.* **2020**, *32*, 1905923.

(25) Calleja, M.; Dove, M. T.; Salje, E. K. H. Trapping of Oxygen Vacancies on Twin Walls of $CaTiO_3$: A Computer Simulation Study. *J. Phys.: Condens. Matter* **2003**, *15*, 2301−2307.

(26) Aird, A.; Salje, E. K. H. Enhanced Reactivity of Domain Walls in with Sodium. *Eur. Phys. J. B* **2000**, *15*, 205−210.

(27) Yan, P.; Zheng, J.; Liu, J.; Wang, B.; Cheng, X.; Zhang, Y.; Sun, X.; Wang, C.; Zhang, J.-G. Tailoring Grain Boundary Structures and Chemistry of Ni-Rich Layered Cathodes for Enhanced Cycle Stability of Lithium-Ion Batteries. *Nat. Energy* **2018**, *3*, 600−605.

(28) Lu, K.; Lu, L.; Suresh, S. Strengthening Materials by Engineering Coherent Internal Boundaries at the Nanoscale. *Science* **2009**, *324*, 349−352.
(29) Ma, C.; Chen, K.; Liang, C.; Nan, C.-W.; Ishikawa, R.; More, K.; Chi, M. Atomic-Scale Origin of the Large Grain-Boundary Resistance in Perovskite Li-Ion-Conducting Solid Electrolytes. *Energy Environ. Sci.* **2014**, *7*, 1638−1642.
(30) Sasano, S.; Ishikawa, R.; Kawahara, K.; Kimura, T.; Ikuhara, Y. H.; Shibata, N.; Ikuhara, Y. Grain Boundary Li-Ion Conductivity in $(Li_{0.33}La_{0.56})TiO_3$ Polycrystal. *Appl. Phys. Lett.* **2020**, *116*, 043901.
(31) Wang, C.; Wang, S.; He, Y.-B.; Tang, L.; Han, C.; Yang, C.; Wagemaker, M.; Li, B.; Yang, Q.-H.; Kim, J.-K.; Kang, F. Combining Fast Li-Ion Battery Cycling with Large Volumetric Energy Density: Grain Boundary Induced High Electronic and Ionic Conductivity in $Li_4Ti_5O_{12}$ Spheres of Densely Packed Nanocrystallites. *Chem. Mater.* **2015**, *27*, 5647−5656.
(32) Nie, A.; Gan, L.-Y.; Cheng, Y.; Li, Q.; Yuan, Y.; Mashayek, F.; Wang, H.; Klie, R.; Schwingenschlogl, U.; Shahbazian-Yassar, R. Twin Boundary-Assisted Lithium Ion Transport. *Nano Lett.* **2015**, *15*, 610−615.
(33) Zhu, X.; Ong, C. S.; Xu, X.; Hu, B.; Shang, J.; Yang, H.; Katlakunta, S.; Liu, Y.; Chen, X.; Pan, L.; et al. Direct Observation of Lithium-Ion Transport under an Electrical Field in Li_xCoO_2 Nanograins. *Sci. Rep.* **2013**, *3*, 1084.
(34) Moriwake, H.; Kuwabara, A.; Fisher, C. A.; Huang, R.; Hitosugi, T.; Ikuhara, Y. H.; Oki, H.; Ikuhara, Y. First-Principles Calculations of Lithium-Ion Migration at a Coherent Grain Boundary in a Cathode Material, $LiCoO_2$. *Adv. Mater.* **2013**, *25*, 618−622.
(35) Lee, H.-S.; Park, C.; Oh, C.-S.; Lee, H.-S.; Seo, H.; Hyun, Y.-T.; Lee, D.-W. Atomic Structure and Defect Energetics of $LiCoO_2$ Grain Boundary. *Mater. Res. Bull.* **2016**, *82*, 81−86.
(36) Whittingham, M. S. Lithium Batteries and Cathode Materials. *Chem. Rev.* **2004**, *104*, 4271−4302.
(37) Nitta, N.; Wu, F.; Lee, J. T.; Yushin, G. Li-Ion Battery Materials: Present and Future. *Mater. Today* **2015**, *18*, 252−264.
(38) Liu, W.; Oh, P.; Liu, X.; Lee, M.-J.; Cho, W.; Chae, S.; Kim, Y.; Cho, J. Nickel-Rich Layered Lithium Transition-Metal Oxide for High-Energy Lithium-Ion Batteries. *Angew. Chem., Int. Ed.* **2015**, *54*, 4440−4457.
(39) Thackeray, M. M.; Kang, S.-H.; Johnson, C. S.; Vaughey, J. T.; Benedek, R.; Hackney, S. A. Li_2MnO_3-Stabilized $LiMO_2$ (M= Mn, Ni, Co) Electrodes for Lithium-Ion Batteries. *J. Mater. Chem.* **2007**, *17*, 3112−3125.
(40) Lee, S.-Y.; Park, G.-S.; Jung, C.; Ko, D.-S.; Park, S.-Y.; Kim, H. G.; Hong, S.-H.; Zhu, Y.; Kim, M. Revisiting Primary Particles in Layered Lithium Transition-Metal Oxides and Their Impact on Structural Degradation. *Adv. Sci.* **2019**, *6*, 1800843.
(41) Sharifi-Asl, S.; Yurkiv, V.; Gutierrez, A.; Cheng, M.; Balasubramanian, M.; Mashayek, F.; Croy, J.; Shahbazian-Yassar, R. Revealing Grain-Boundary-Induced Degradation Mechanisms in Li-Rich Cathode Materials. *Nano Lett.* **2020**, *20*, 1208−1217.
(42) Qian, G.; Zhang, Y.; Li, L.; Zhang, R.; Xu, J.; Cheng, Z.; Xie, S.; Wang, H.; Rao, Q.; He, Y.; et al. Single-Crystal Nickel-Rich Layered-Oxide Battery Cathode Materials: Synthesis, Electrochemistry, and Intra-Granular Fracture. *Energy Stor. Mater.* **2020**, *27*, 140−149.
(43) Liu, H.; Wolf, M.; Karki, K.; Yu, Y.-S.; Stach, E. A.; Cabana, J.; Chapman, K. W.; Chupas, P. J. Intergranular Cracking as a Major Cause of Long-Term Capacity Fading of Layered Cathodes. *Nano Lett.* **2017**, *17*, 3452−3457.
(44) Gong, Y.; Zhang, J.; Jiang, L.; Shi, J.-A.; Zhang, Q.; Yang, Z.; Zou, D.; Wang, J.; Yu, X.; Xiao, R.; et al. In Situ Atomic-Scale Observation of Electrochemical Delithiation Induced Structure Evolution of $LiCoO_2$ Cathode in a Working All-Solid-State Battery. *J. Am. Chem. Soc.* **2017**, *139*, 4274−4277.
(45) Kresse, G.; Furthmüller, J. Efficient Iterative Schemes for Ab Initio Total-Energy Calculations Using a Plane-Wave Basis Set. *Phys. Rev. B: Condens. Matter Mater. Phys.* **1996**, *54*, 11169.
(46) Blöchl, P. E. Projector Augmented-Wave Method. *Phys. Rev. B: Condens. Matter Mater. Phys.* **1994**, *50*, 17953.
(47) Perdew, J. P.; Burke, K.; Ernzerhof, M. Generalized Gradient Approximation Made Simple. *Phys. Rev. Lett.* **1996**, *77*, 3865−3868.
(48) Aykol, M.; Kim, S.; Wolverton, C. Van Der Waals Interactions in Layered Lithium Cobalt Oxides. *J. Phys. Chem. C* **2015**, *119*, 19053−19058.
(49) Dixit, M.; Kosa, M.; Lavi, O. S.; Markovsky, B.; Aurbach, D.; Major, D. T. Thermodynamic and Kinetic Studies of $LiNi_{0.5}Co_{0.2}Mn_{0.3}O_2$ as a Positive Electrode Material for Li-Ion Batteries Using First Principles. *Phys. Chem. Chem. Phys.* **2016**, *18*, 6799−6812.
(50) Henkelman, G., Jóhannesson, G., Jónsson, H. In *Theoretical Methods in Condensed Phase Chemistry*; Schwartz, S. D., Eds.; Springer: Dordrecht, 2002; Vol. *5*, pp 269−302.
(51) Henkelman, G.; Uberuaga, B. P.; Jónsson, H. A Climbing Image Nudged Elastic Band Method for Finding Saddle Points and Minimum Energy Paths. *J. Chem. Phys.* **2000**, *113*, 9901−9904.
(52) Urban, A.; Seo, D.-H.; Ceder, G. Computational Understanding of Li-Ion Batteries. *npj Comput. Mater.* **2016**, *2*, 16002.
(53) Chakraborty, A.; Kunnikuruvan, S.; Kumar, S.; Markovsky, B.; Aurbach, D.; Dixit, M.; Major, D. T. Layered Cathode Materials for Lithium-Ion Batteries: Review of Computational Studies on $LiNi_{1-x-y}Co_xMn_y$ O_2 and $LiNi_{1-x-y}Co_xAl_yO_2$. *Chem. Mater.* **2020**, *32*, 915−952.
(54) Mueller, T.; Hautier, G.; Jain, A.; Ceder, G. Evaluation of Tavorite-Structured Cathode Materials for Lithium-Ion Batteries Using High-Throughput Computing. *Chem. Mater.* **2011**, *23*, 3854−3862.
(55) *Grain Boundaries: From Theory to Engineering*; Priester, L.; Springer: New York, 2012.
(56) Glass, C. W.; Oganov, A. R.; Hansen, N. USPEX—Evolutionary Crystal Structure Prediction. *Comput. Phys. Commun.* **2006**, *175*, 713−720.
(57) Sun, H.; Zhao, K. Electronic Structure and Comparative Properties of $LiNi_xMn_yCo_zO_2$ Cathode Materials. *J. Phys. Chem. C* **2017**, *121*, 6002−6010.
(58) Sutton, A. P. Interfaces in Crystalline Materials. *Monogr. Phys. Chem. Mater.* **1995**, 414−423.
(59) Van der Ven, A.; Aydinol, M. K.; Ceder, G.; Kresse, G.; Hafner, J. First-Principles Investigation of Phase Stability in Li_xCoO_2. *Phys. Rev. B: Condens. Matter Mater. Phys.* **1998**, *58*, 2975−2987.
(60) Wei, Y.; Zheng, J.; Cui, S.; Song, X.; Su, Y.; Deng, W.; Wu, Z.; Wang, X.; Wang, W.; Rao, M.; et al. Kinetics Tuning of Li-Ion Diffusion in Layered $Li(Ni_xMn_yCo_z)O_2$. *J. Am. Chem. Soc.* **2015**, *137*, 8364−8367.
(61) Aurbach, D.; Srur-Lavi, O.; Ghanty, C.; Dixit, M.; Haik, O.; Talianker, M.; Grinblat, Y.; Leifer, N.; Lavi, R.; Major, D. T.; et al. Studies of Aluminum-Doped $LiNi_{0.5}Co_{0.2}Mn_{0.3}O_2$: Electrochemical Behavior, Aging, Structural Transformations, and Thermal Characteristics. *J. Electrochem. Soc.* **2015**, *162*, A1014−A1027.
(62) Hua, W.; Zhang, J.; Zheng, Z.; Liu, W.; Peng, X.; Guo, X.-D.; Zhong, B.; Wang, Y.-J.; Wang, X. Na-Doped Ni-Rich $LiNi_{0.5}Co_{0.2}Mn_{0.3}O_2$ Cathode Material with Both High Rate Capability and High Tap Density for Lithium Ion Batteries. *Dalton Trans.* **2014**, *43*, 14824−14832.
(63) Vineyard, G. H. Frequency Factors and Isotope Effects in Solid State Rate Processes. *J. Phys. Chem. Solids* **1957**, *3*, 121−127.
(64) Gong, X.; Huang, J. M.; Chen, Y.; Wu, M. S.; Liu, G.; Lei, X.; Liang, J.; Cao, H.; Tang, F.; Xu, B. Vibrational Contribution to the Thermodynamic Properties of Lithium Ion Batteries System: A First Principles Calculations. *Int. J. Electrochem. Sci.* **2013**, *8*, 10549−10556.
(65) Van der Ven, A.; Thomas, J. C.; Xu, Q.; Swoboda, B.; Morgan, D. Nondilute Diffusion from First Principles: Li Diffusion in Li_xTiS_2. *Phys. Rev. B: Condens. Matter Mater. Phys.* **2008**, *78*, 104306.
(66) Van der Ven, A.; Ceder, G.; Asta, M.; Tepesch, P. D. First-Principles Theory of Ionic Diffusion with Nondilute Carriers. *Phys. Rev. B: Condens. Matter Mater. Phys.* **2001**, *64*, 184307.
(67) Kutner, R. Chemical Diffusion in the Lattice Gas of Non-Interacting Particles. *Phys. Lett. A* **1981**, *81*, 239−240.

https://doi.org/10.1021/acs.jpcc.1c02400
J. Phys. Chem. C 2021, 125, 10284−10294

(68) Jamnik, J.; Maier, J. Generalised Equivalent Circuits for Mass and Charge Transport: Chemical Capacitance and Its Implications. *Phys. Chem. Chem. Phys.* **2001**, *3*, 1668−1678.
(69) Dawson, J. A.; Canepa, P.; Famprikis, T.; Masquelier, C.; Islam, M. S. Atomic-Scale Influence of Grain Boundaries on Li-Ion Conduction in Solid Electrolytes for All-Solid-State Batteries. *J. Am. Chem. Soc.* **2018**, *140*, 362−368.
(70) Choi, M.-H.; Yoon, C. S.; Myung, S.-T.; Lim, B.-B.; Komaba, S.; Sun, Y.-K. Effect of Lithium in Transition Metal Layers of Ni-Rich Cathode Materials on Electrochemical Properties. *J. Electrochem. Soc.* **2015**, *162*, A2313−A2318.

https://doi.org/10.1021/acs.jpcc.1c02400
J. Phys. Chem. C 2021, 125, 10284−10294